How crucial is the impact of calcium on the reactivity of iron-organic matter aggregates? Insights from arsenic

Anthony Beauvois, Delphine Vantelon, Jacques Jestin, Martine Bouhnik-Le Coz, Charlotte Catrouillet, Valérie Briois, Thomas Bizien, Mélanie Davranche

How crucial is the impact of calcium on the reactivity of iron-organic matter aggregates? Insights from arsenic

Anthony Beauvois, Delphine Vantelon, Jacques Jestin, Martine Bouhnik-Le Coz, Charlotte Catrouillet, Valérie Briois, Thomas Bizien, Mélanie Davranche

PII: S0304-3894(20)32117-8

DOI: https://doi.org/10.1016/j.jhazmat.2020.124127

Reference: HAZMAT124127

To appear in: *Journal of Hazardous Materials*

Received date: 9 July 2020
Revised date: 16 September 2020
Accepted date: 26 September 2020

Please cite this article as: Anthony Beauvois, Delphine Vantelon, Jacques Jestin, Martine Bouhnik-Le Coz, Charlotte Catrouillet, Valérie Briois, Thomas Bizien and Mélanie Davranche, How crucial is the impact of calcium on the reactivity of iron-organic matter aggregates? Insights from arsenic, *Journal of Hazardous Materials,* (2020) doi:https://doi.org/10.1016/j.jhazmat.2020.124127

How crucial is the impact of calcium on the reactivity of iron-organic matter aggregates? Insights from arsenic

Anthony Beauvois[a,b,c*], Delphine Vantelon[b], Jacques Jestin[c,⁑], Martine Bouhnik-Le Coz[a], Charlotte Catrouillet[a], Valérie Briois[b], Thomas Bizien[b] and Mélanie Davranche[a]

[a]*Univ. Rennes, CNRS, Géosciences Rennes - UMR 6118, F-35000 Rennes, France*

[b]*Synchrotron SOLEIL, L'Orme des Merisiers, Saint-Aubin BP48, 91192 Gif-sur-Yvette Cedex*

[c]*Laboratoire Léon Brillouin, CEA Saclay, 91191 Gif-sur-Yvette Cedex*

[*]*Corresponding author: anthony.beauvois@univ-rennes1.fr*

[⁑]*Present address: Institut Laue-Langevin, 6 rue Jules Horowitz, 38000 Grenoble, France*

Abstract

Environmental iron-organic matter (Fe-OM) aggregates play a major role in the dynamic of pollutants. Nowadays, there is a lack of information about the control exerted by their structural organization on their reactivity towards metal(loid)s and in particular, the impact of major ions, such as calcium. The sorption capacity of mimetic environmental Fe-OM-Ca aggregates was investigated relative to the Fe/organic carbon (OC) and Ca/Fe ratios using As as a probe. It was shown that Fe speciation is the key factor controlling the reactivity of Fe-OM-Ca aggregates regarding the high affinity of Fe(III)-oligomers towards As and the high sorption capacity of ferrihydrite-like nanoparticles. Moreover, when it occurs at high concentration, Ca competes with Fe for OM binding leading to an increase in the amount of ferrihydrite-like nanoparticles and binding site availability. As a consequence, Ca not only

impacts the ionic strength but it also has a dramatic impact on the structural organization of Fe-OM aggregates at several scales of organization, resulting in an increase of their sorption capacity. In the presence of high amounts of Ca, Fe-OM-Ca aggregates could immobilize pollutants in the soil porous media as they form a micrometric network exhibiting a strong sorption capacity.

Graphical Abstract

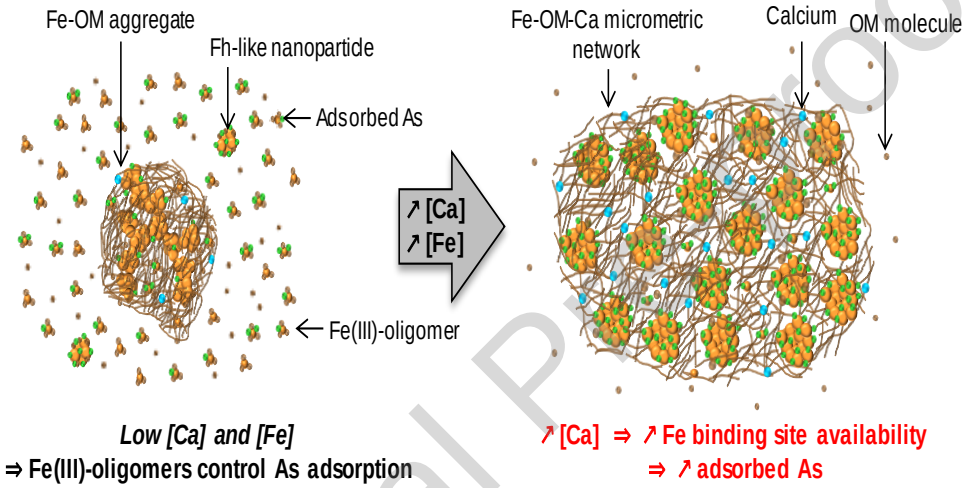

Keywords

Fe-OM colloids, adsorption isotherms, ferrihydrite, Fe-oligomers, EXAFS, SAXS, Ca interactions.

1. Introduction

Environmental colloids are of major importance given their high reactivity towards metal and metalloid pollutants [1]. They are nanometric particles, either aggregated or not, with a high specific surface area (SSA), mainly composed of minerals and/or organic matter (OM). Among them, those particles composed of iron (Fe) and OM, usually called "iron-organic matter (Fe-OM) aggregates", are widely encountered in natural systems such as wetlands where they are mainly produced by drying/wetting cycles in the uppermost soils [2–6].

For many years, the structure and organization of Fe-OM aggregates ~~was~~ were only simply described as poorly crystallized iron oxyhydroxides embedded in an OM matrix [7]. The overall multiscale complexity of the organization between Fe and OM was poorly investigated. Only recently, several studies have demonstrated that within Fe-OM aggregates, OM in the form of molecules and colloidal aggregates [3,8,9] constrains the growth and crystallinity of the Fe phases [10,11]. The result is that Fe forms Fe(III) monomers, small oligomers and ferrihydrite-like nanoparticles (Fh-like Nps), bound to the OM involving its carboxylic (COOH) and phenolic (PhOH) sites [8,11–16]. Fh-like Nps exhibit a fractal organization, composed of primary beads (radius ~0.8 nm) forming primary aggregates (radius ~4 nm) that can aggregate to form secondary aggregates (radius > 100 nm) bound to large OM aggregates [3,8]. As a consequence, despite the fact that they are known to react strongly with pollutants, many questions still remain with regards to the binding capacities of such heterogeneous and polymorph aggregates. For many years, it was accepted that the sorption capacities of such entities follow an additive rule, i.e. for a given chemical element, the total sorption capacity was the sum of the ability of the components of each aggregate to sorb this element. However, although some experimental data ~~was~~ were successfully modelled and reproduced following this additive model [17,18], many other data were not

[19–22]. As an example, Weng et al. [23] observed an additivity behavior for fulvic acid and goethite while Christl and Kretzschmar [24] observed a non-additive behavior for fulvic acid and hematite. The most probable explanation is that the structural organization between components strongly influences the global surface reactivity of the aggregate (e.g. in response to the surface covering). More recently, Guénet et al. [3] demonstrated that the sorption capacity of the Fe-OM aggregates increased with the increasing Fe/organic carbon (OC) ratio while the SSA of the Fe-NPs remained constant, providing evidence that SSA was not the only parameter that controls the reactivity of Fe-OM aggregates towards chemical elements. These authors considered that with the increasing Fe/OC ratio, the distance between the Fe primary aggregates within the Fe secondary aggregates ~~increases~~ increased, and that this involved a decrease in the Fe coating rate by the OM and an increase in the availability of the binding sites. In light of the recent evidence in support of the ~~Fe-OM~~ structural and organizational complexity of Fe-OM aggregates, these results bring the simplistic additive model into question and highlight the importance of the structural organization of Fe-OM aggregates in their sorption reactivity towards chemical elements.

Furthermore, in natural systems, major ions such as Ca coexist with Fe and OM [25]. In a recent study, we demonstrated that Ca can strongly influence the structural organization of the Fe-OM aggregates, depending on the Ca concentration [8]. When low amounts of Ca are present, the overall structural organization of the Fe-OM aggregates is not modified. By contrast, for high Ca concentrations (i.e. Ca/OC $\geq$ 0.026), Ca drives the structural transition of the Fe-OM aggregates from a colloidal state to a non-colloidal micrometric Ca-branched OM network in which Fh-like Nps remained embedded. This dramatic change ~~is~~ mainly ~~involved~~ occurs through the binding of Ca to the OM COOH sites. For high amounts of Ca, the divalent cation could thus compete against metals and metalloids for OM binding. In these conditions, the interactions between Fe and OM are partially screened and two antagonist

results are expected: ~~an increase in the availability of Fe binding sites, free from OM, or an increase in the size of the Fh-like Nps [8,26] involving a decrease in their SSA and subsequently, their decreased sorption capacity~~. Iron reactive sites are free from OM leading to an increase their binding site availability. Moreover the size of the Fh-like Nps increases [8,26] involving a decrease in their SSA and a subsequent decrease of their sorption capacity.

To understand the overall adsorption capacity of the Fe-OM aggregates, it is necessary to investigate the reactivity of the Fe and OM phases independently. In the present study, we investigate the reactivity of the Fe phases within Fe-OM aggregates at several Fe/~~organic carbon (OC)~~OC and Ca/Fe ratios. Thus, our goal is to provide a clear description of the parameters that control their sorption capacity. For this purpose, arsenic (As) was used as a probe of the ~~Fe~~ surface reactivity of Fe as ~~it~~ arsenic is known to have a stronger affinity for Fe than for OM. Iron-OM-Ca aggregates were synthesized at various Fe/OC and Ca/Fe ratios. The speciation of Fe was studied by X-ray absorption spectroscopy (XAS) at the Fe K-edge and the size and specific surface of the particulate Fe in the Fe-OM-Ca aggregates ~~was~~ were investigated using small-angle X-ray scattering (SAXS). To evaluate the binding capacity of the Fe-OM aggregates and the parameters controlling this process, As sorption experiments were carried out and coupled with (ultra)filtrations to investigate the distribution of As relative to the size evolution of the Fe-OM aggregates.

2. Materials and methods

2.1. Sample syntheses and chemical analyses

2.1.1. Sample synthesis

~~Samples were synthesized at three Fe/OC ratios (0.02, 0.05 and 0.08 mol./mol.) and four Ca/Fe ratios (0, 0.1, 0.5 and 1 mol./mol.) following the procedure described by Guénet et al. [3]. Samples are labelled Fe*xx*-Ca*yy*, where *xx* and *yy* represent the Fe/OC and Ca/Fe~~

~~ratios, respectively. The OM used was Leonardite Humic Acid (LHA) purchased from the international humic substance society (IHSS) with the following elemental composition C = 63.81%, O = 31.27%, H = 3.70% and N = 1.23% (as mass fraction). An iron(II) stock solution of 1.79×10^{-2} mol L^{-1} was prepared with $FeCl_2.4H_2O$ (Sigma Aldrich). From this solution, three Fe(II)-Ca(II) solutions were prepared at [Ca] = 2.50×10^{-3} mol L^{-1}, 1.25×10^{-2} mol L^{-1} and 2.50×10^{-2} mol L^{-1} with $CaCl_2.2H_2O$ (Sigma Aldrich). The Fe-OM-Ca aggregates were synthesized through a titration of the LHA suspension at [OC] = 1.00×10^{-1} mol L^{-1} with the Fe(II)-Ca(II) solution at 0.05 mL min^{-1} in 5×10^{-3} mol L^{-1} of NaCl using an automated titrator (Titrino 794, Metrohm). The pH was monitored at 6.5 ± 0.04 with a 0.1 M NaOH solution using a second titrator (Titrino 794, Metrohm) at a set pH mode. A solution of pure LHA was prepared by dissolving 25 mg of the LHA in a 1×10^{-3} mol L^{-1} NaCl solution at pH = 6.0 as a reference for the chemical analyses.~~

The Fe-OM-Ca aggregates were synthesized following the procedure described by Guénet et al. [3] and Beauvois et al. [8]. The Leonardite Humic Acid (LHA), purchased from the international humic substance society (IHSS), was used as the OM and has the following elemental composition C = 63.81%, O = 31.27%, H = 3.70% and N = 1.23% (as mass fraction). A LHA solution at [OC] = 1.00×10^{-1} mol L^{-1} was prepared by dissolving the powder at pH = 9. After being stirred for 24 h, the pH of the LHA stock solution was adjusted to 6.5 using a 1 mol L^{-1} HCl solution. An iron(II) stock solution of 1.79×10^{-2} mol L^{-1} was prepared with $FeCl_2.4H_2O$ (Sigma Aldrich) at pH = 2 to avoid Fe(II) oxidation. From this solution, three Fe(II)-Ca solutions were prepared adding $CaCl_2.2H_2O$ powder (Sigma Aldrich) to reach [Ca] = 2.50×10^{-3} mol L^{-1}, 1.25×10^{-2} mol L^{-1} and 2.50×10^{-2} mol L^{-1}, that corresponds to Ca/Fe molar ratios of 0.1, 0.5 and 1, respectively. The ionic strength of all of the solutions was fixed with 5×10^{-3} mol L^{-1} of NaCl. The synthesis of the samples consisted of titrating the LHA solution with the Fe(II) or the Fe(II)-Ca solutions at 0.05 mL min^{-1} using an automated titrator

(Titrino 794, Metrohm). The added volume of the Fe(II) or the Fe(II)-Ca solutions was determined in order to reach three Fe/OC molar ratios (0.02, 0.05 and 0.08). During the synthesis, the pH was monitored at 6.5 ± 0.04 with a 0.1 mol L^{-1} NaOH solution using a second titrator (Titrino 794, Metrohm) in a set pH mode. The samples were labelled Fe*xx*-Ca*yy*, where *xx* and *yy* represent the Fe/OC and Ca/Fe ratios, respectively.

2.1.2. Arsenic sorption experiments

Arsenic sorption isotherms were performed in triplicate for all of the samples ~~at~~ for five As/Fe ratios (i.e. 0.0007, 0.004, 0.04, 0.15 and 0.4 mol/mol). For this purpose, various As(III) solutions were prepared from $NaAsO_2$ (Sigma Aldrich) at 5.00×10^{-2} mol L^{-1}, 5.00×10^{-3} mol L^{-1} and 5.00×10^{-4} mol L^{-1}. An aliquot of each As(III) solution was added to the suspension of Fe-OM-Ca aggregates to reach the ~~fixed~~ set As/Fe ratio. The pH of the suspensions was adjusted to 6.5 ± 0.04 using 1 mol L^{-1} HCl or NaOH. The equilibrium time for As adsorption onto goethite ~~in the presence of~~ with HA and onto hematite nanoparticles was ~~demonstrated~~ reported to be 4 h and 24 h, respectively [27,28]. Similarly, Raven et al. [29] observed an equilibrium time for the ~~As~~ adsorption of As by Fh of 24 h, irrespective of the pH or the initial As concentration. The suspensions were therefore stirred for 24 h to ensure that the equilibrium is reached. A fraction of each solution was ultrafiltrated at 30 kDa (Vivaspin VS2022, Sartorius). The ultrafiltrate corresponds to the dissolved species. The arsenic concentration was measured in the bulk fraction and in the <30 kDa fraction in order to determine the quantity of adsorbed As on Fe phases.

For an As/Fe ratio = 0.004 and 0.15, additional (ultra)filtrations were performed at 0.2 µm (cellulose acetate membrane filter, Sartorius), 1000 kDa (Vivaspin VS2062, Sartorius) and 100 kDa (Vivaspin VS2042, Sartorius). Each 0.2 µm filter was rinsed with 200 mL of Milli-Q water (Millipore) before use. Each ultrafiltration cell was washed several times with 15 mL of a 0.1 mol L^{-1} NaOH solution and Milli-Q water until the DOC concentration in the

ultrafiltrate was below 0.2 mg L^{-1}. An As/Fe ratio = 0.004 was chosen since it is close to the ratio observed in riparian wetland soil solutions [30,31] and an As/Fe ratio = 0.15 was chosen because it ensured a high As adsorption rate [3,32].

2.1.3. Chemical analyses

The chemical analyses were performed on the bulk fraction and all of the (ultra)filtrates. The OC concentrations were determined using an OC analyzer (Shimadzu TOC-V CSH). The uncertainty of the C measurement was determined to be ± 5% using a standard solution of potassium hydrogen phthalate (Sigma Aldrich). The Fe, Ca and As concentrations were measured by inductively coupled plasma mass spectrometry (ICP-MS) using an Agilent Technologies 7700x instrument at the University of Rennes 1. In order to solubilize the Fe, Ca and As and to eliminate the OM, the samples were predigested with 14.6 mol L^{-1} distilled HNO_3 at 90°C and evaporated. A second oxidative predigestion with a mixture of 14.6 mol L^{-1} distilled HNO_3 and Suprapur 30% H_2O_2 (a HNO_3/H_2O_2 volume ratio of ~75/25) at 90°C was necessary to completely dissolve the samples. ~~Finally~~ Lastly, the samples were evaporated to complete dryness and solubilized with HNO_3 at 0.37 mol L^{-1} prior to the ICP-MS measurements. The detection limits of the ICP-MS measurements were 1×10^{-2}, 2×10^{-3} and 5×10^{-5} mol L^{-1} for Ca, Fe and As, respectively.

All of the aqueous solutions were prepared with Milli-Q water (Millipore).

2.2. Adsorption isotherm modelling

~~As adsorption isotherms were fitted with the Langmuir equation (eq. 1):~~ The adsorption isotherms were fitted with the Freundlich and Langmuir isotherm. The Langmuir isotherm results were significantly better than for Freundlich isotherm, as previously observed for several Fe (hydr)oxides sorption studies [33]. The Langmuir model was therefore used in the present sutdy. It can be described by the following equation (eq. 1):

$$q = \frac{q_{max}.K_{ads}.C}{1 + K_{ads}.C} \quad \text{(eq. 1)}$$

where q is the quantity of adsorbed As per unit mass of adsorbent (µmol g^{-1}), q_{max} is the maximal quantity of adsorbed As per unit mass of adsorbent (µmol g^{-1}), Langmuir K_{ads} is a constant related to the binding strength of adsorbent (L µmol^{-1}) and C is the final concentration of As in solution (µmol L^{-1}), i.e. in the <30 kDa fraction as described above [34]. The isotherms were fitted using the KaleidaGraph software with the Levenberg-Marquardt algorithm in order to calculate the best curve fit using an iterative procedure.

2.3. Fe K-edge XAS data acquisition and analysis

~~Before the adsorption experiments were performed, a fraction of~~ Prior to the adsorption experiments, an aliquot of each sample was freeze dried (Freeze dryer Alpha 1-2 LD plus, Christ). The powder was then mixed with cellulose (Merck) and pressed into a 6 mm pellet. The Fe K-edge spectra were recorded on the ROCK [35] beamline at the SOLEIL synchrotron (Saint-Aubin, France). The monochromator used was a Si(111) channel-cut. The spectra were recorded in transmission mode using three ionization chambers (Ohyo Koken) filled with N_2. The energy was calibrated using a Fe foil located between the 2nd and 3rd ionization chambers and measured simultaneously with the samples. The calibration was done by setting the maximum of the first derivate of the Fe foil to 7112 eV. The reference used for ~~further~~ the subsequent data analysis was a Fh synthesized ~~following~~ as per the procedure described in Schwertmann and Cornell [36].

All of the XAS data were processed using the Athena software [37] including the Autbk algorithm (Rbkb = 1, k-weight = 3). The Fe spectra were normalized by fitting the pre-edge region with a linear function and the post-edge region with a quadratic polynomial function. The Fourier transforms of the k^3-weighted EXAFS spectra were calculated over a range of 2-12.5 $Å^{-1}$ using a Hanning apodization window (window parameter = 1). Back Fourier filters were extracted over the R-range of 1.15-4.1 Å, using the same apodization window shape. The EXAFS data were analyzed by linear combination fitting (LCF) procedure available in

the Athena software over the range 3-12.5 $Å^{-1}$; all the component weights were forced to be positive. Beauvois et al. [8] demonstrated that the EXAFS data at the Fe K-edge could be reproduced by performing LCF using Fe(III)-oligomers and Fe(III)-Np isolated by Vantelon et al. [11] as well as Fh. The total LCF weight for each sample varied between 0.95 and 1.05 without any constraint. In order to facilitate the comparison between each sample, the total LCF weight was arbitrary fixed to 1. The EXAFS data were also fitted in the range 1.15-4.1 Å with the Artemis [37] interface to IFEFFIT using a least-squares refinement procedure. The theoretical backscattering paths used were calculated from a goethite structure [38] using the FEFF6 algorithm [39] included in the Artemis interface.

2.4. SAXS measurements

The small-angle X-ray scattering measurements were performed on the SWING beamline at the SOLEIL synchrotron. Using two sample-to-detector distances (1 and 6 m) at a wavelength of 1.03 Å, a momentum transfer q range of 2.0×10^{-3}-0.7 $Å^{-1}$ was reached using a EIGERX 4M detector. Measurements were also carried out on the XEUSS 2.0 spectrometer from Xenocs (CEA-LIONS/LLB, Saclay, France). With two sample-to-detector distances (0.33 and 2.49 m) and a wavelength of 1.54 Å (Cu X-ray source), a momentum transfer range of 4.5×10^{-3}-0.5 $Å^{-1}$ was reached.

In the high q domain of the SAXS curves, the so-called Porod region, the scattered intensity is proportional to the surface scattering per unit volume S/V and can be modelled according to the following equation (eq. 2):

$$\lim\big(I(q)\big) = \frac{2\pi\varphi_0\Delta\rho^2}{q^4}\frac{S}{V} \qquad \text{(eq. 2)}$$

where φ_0 is the volume fraction of the primary beads, $\Delta\rho^2$ is the contrast term (cm^{-4}), both ~~estimated~~ determined by Beauvois et al. [8]. By dividing S/V by the mean density of the Fe aggregates (i.e. 3.96 g cm^{-3} [40]), we were able to calculate the SSA of the Fh-like Nps.

3. Results

3.1. OC, Fe, Ca and As distribution in the size fractions

The OC, Ca, Fe and As concentrations in each fraction are reported in Tables SI 1-7, respectively. For the samples at the Ca/Fe ratio = 0, 0.11 mmol L^{-1} of Ca was detected which corresponded to the concentration of Ca naturally present in the LHA (Table SI 8). The ICP-MS measurements of the LHA alone also displayed [Fe] = 0.04 mmol L^{-1}, which is low as compared to the lowest Fe/OC ~~with~~ in which [Fe] = 1.23 mmol L^{-1} and [As] was below the detection limit.

The % distribution of OC, Ca, Fe and As in each size fraction is reported in Figure 1 (for As/Fe = 0.004) and Figure SI-1 (for As/Fe = 0.15). In the <30 kDa fraction, ~5% of the OC and less than 1% of the Fe were present. The dissolved As% decreased with the increasing Fe/OC ratio for all of the Ca/OC ratios. By contrast, irrespective of the Fe/OC ratio, the Ca% in the <30 kDa fraction remained < 10% for the Ca/Fe ratios ≤ 0.1. Then, it increased with the increasing Ca/Fe ratio. This increase was less pronounced for Fe/OC = 0.02 compared to Fe/OC ≥ 0.05. The results provided evidence of a perfect co-distribution of OC, Ca, Fe and As in the >30 kDa fractions. For Fe/OC = 0.02, ~80% of the OC, Ca, Fe and As in the >30 kDa fraction were distributed in the 1000-100 kDa fraction, ~15% were in the >0.2 µm fraction and the remaining 5% were distributed in the other fractions for both Ca/Fe = 0 and 0.1. With the increasing Ca/Fe ratio, the amount of OC, Ca, Fe and As in the 1000-100 kDa fraction decreased until ~60% for Ca/Fe = 1, and simultaneously increased in the >0.2 µm fraction (~30%) and to a lower extent in the 0.2 µm-1000 kDa fraction (~10%). The same behavior was observed for the higher Fe/OC values. For Fe/OC = 0.05, with the increasing Ca/OC ratio from 0 to 0.1, the proportion of OC, Ca, Fe and As decreased from ~75% to ~65% ~~from~~ between the 1000-100 kDa fraction and ~~to~~ the >0.2 µm fraction for which the % increased from ~20% to ~30%. For Ca/Fe = 0.5, the concentration was below the

ICP-MS detection limit in the 1000-100 kDa fraction while ~30% and ~65% were observed in the 0.2 µm-1000 kDa and >0.2 µm fractions, respectively. This distribution was higher for Ca/Fe = 1, as almost all of the OC, Fe, Ca and As ~~were~~ was distributed in the >0.2 µm fraction. For the highest Fe/OC = 0.08, OC, Fe, Ca and As in the 1000-100 kDa fraction decreased from ~60% for Ca/Fe = 0 to ~0% for Ca/Fe ≥ 0.5 and increased in the >0.2 µm fraction, which reached 100% for Ca/Fe ≥ 0.5.

In summary, for Ca/Fe = 0, OC, Fe, Ca and As primarily occurred ~~mainly~~ in the 1000-100 kDa fraction. When the [Fe] and [Ca] increased, ~~they~~ OC, Fe, Ca and As were transferred to the >0.2 µm fraction. ~~The Ca/Fe ratio had a greater influence than that of Fe/OC.~~ The [Ca] had a greater influence than that of [Fe]. This result is illustrated in Figure SI-2 by plotting the evolution of the As % distributed in the 1000-100kDa fraction relative to [Fe] and [Ca]. Therefore, the size of the Fe-OM-Ca association increased with the increasing Ca concentration.

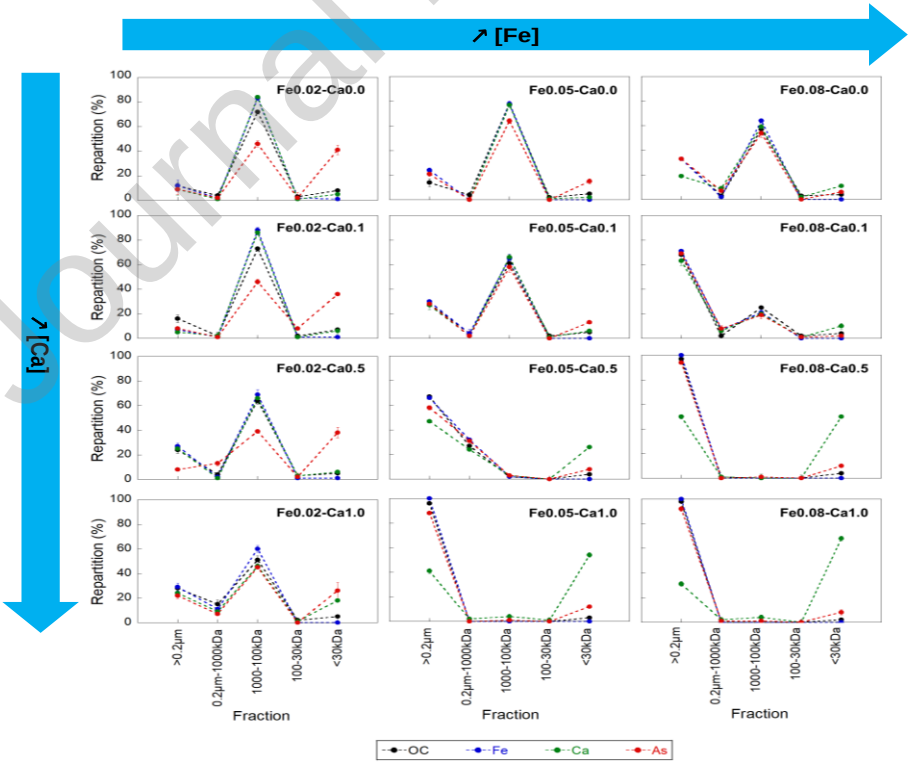

Figure 1 – Percentage of the ~~distribution of~~ OC (black), Fe (blue), Ca (green) and As (red) distributions relative to the size fraction for each Fe/OC and Ca/OC ratio at As/Fe = 0.004.

3.2. Arsenic adsorption isotherms

The As adsorption isotherms exhibited an L-type curve shape for which the slope decreased with the increasing As concentration. The isotherms were fitted with the Langmuir equation (eq. 1) (Figure 2, Table 1). The good quality of the fit ($R^2 > 0.975$) demonstrated that the Langmuir isotherm is suitable for As sorption by the Fe-OM-Ca aggregates.

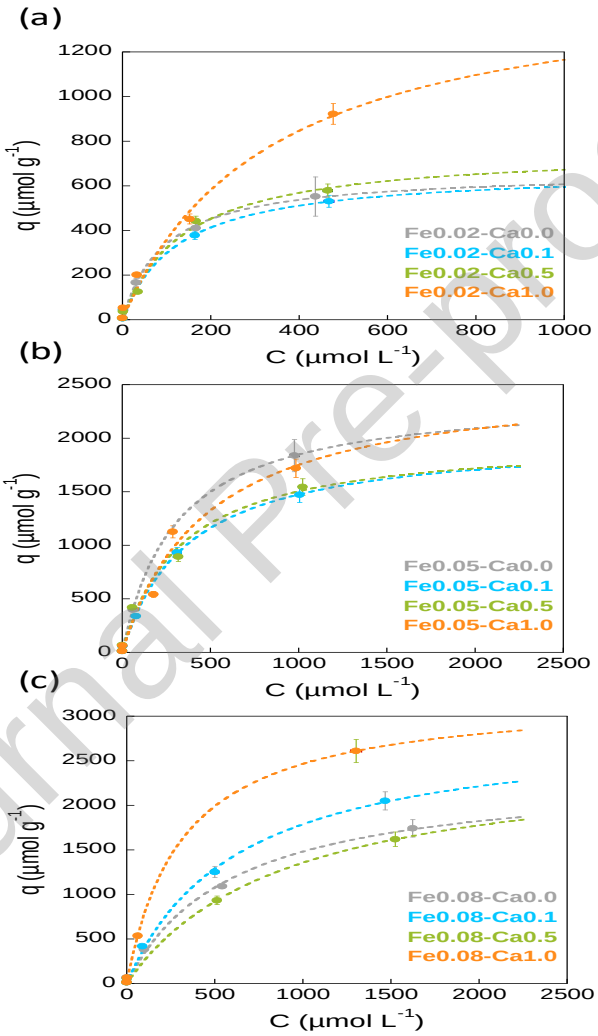

Figure 2 – Arsenic adsorption isotherms for (a) Fe/OC = 0.02, (b) Fe/OC = 0.05 and (c) Fe/OC = 0.08. The circles represent the experimental points and the dotted lines represent the Langmuir isotherm.

The Fe-OM-Ca aggregates exhibited a sorption capacity, q_{max}, varying from ~665 µmol g^{-1} for Fe0.02-Ca0.0 to 3240 µmol g^{-1} for Fe0.08-Ca1.0. The q_{max} value increased with the increasing Fe/OC ratio. These q_{max} were in the range of those calculated for Fh under similar pH conditions (Table 2). However, they ~~are~~ were around one order of magnitude

higher than crystallized Fe-oxides such as magnetite or goethite (Table 2). By contrast, the Langmuir K_{ads} value for the Fe-OM-Ca aggregates ~~Langmuir K_{ads}~~ decreased with the increasing Fe/OC ratio. For the Fe/OC ratio = 0.02, the Langmuir K_{ads} value decreased with the increasing Ca/Fe ratio while remaining constant irrespective of the Ca/Fe ratio for Fe/OC ≥ 0.05. The calculated Langmuir K_{ads} values are 10 times lower than those reported for Fh. For the lowest Fe/OC and Ca/Fe ratios, the Langmuir K_{ads} values ~~are~~ were similar to the Langmuir K_{ads} values for Fh bound with OM, but decreased by one order of magnitude with the ~~decreasing~~ increasing Fe/OC and Ca/Fe ratios. Xue et al. [41] demonstrated that the increase in the amount of OM leads to a decrease in the ~~Fh~~ Langmuir K_{ads} value for Fh. Thus, the presence of OM and Ca may be responsible for the decrease in the Langmuir K_{ads} ~~of~~ value for As caused by the Fe Ca-OM aggregates.

Table 1 – Parameters used to fit the adsorption isotherms with the Langmuir model.

Sample	**q_{max} (µmol g^{-1})**	**Langmuir K_{ads} (L µmol^{-1})**	**R^2**
Fe0.02-Ca0.0	6.7×10^{2}	10×10^{-3}	0.995
Fe0.02-Ca0.1	6.7×10^{2}	8×10^{-3}	0.993
Fe0.02-Ca0.5	7.6×10^{2}	7×10^{-3}	0.991
Fe0.02-Ca1.0	1.5×10^{3}	3×10^{-3}	0.986
Fe0.05-Ca0.0	2.4×10^{3}	3×10^{-3}	0.999
Fe0.05-Ca0.1	2.0×10^{3}	3×10^{-3}	0.998
Fe0.05-Ca0.5	2.0×10^{3}	3×10^{-3}	0.983
Fe0.05-Ca1.0	2.6×10^{3}	2×10^{-3}	0.975
Fe0.08-Ca0.0	2.4×10^{3}	2×10^{-3}	0.997
Fe0.08-Ca0.1	2.9×10^{3}	2×10^{-3}	0.998
Fe0.08-Ca0.5	2.6×10^{3}	1×10^{-3}	0.998
Fe0.08-Ca1.0	3.2×10^{3}	3×10^{-3}	0.999

Table 2 – q_{max} and Langmuir K_{ads} of various Fe-oxyhydroxides.

Fe oxyhydroxides	q_{max} (µmol g^{-1})	Langmuir K_{ads}	Experimental conditions	Reference
Fh	1.1×10^{3}	7.0×10^{-2}	pH = 6.0 IS* = 0.02	Zhu et al. [42]
Fh	5.0×10^{3}	1.5×10^{-2}	pH = 7.0 IS* = 0.01	Xue et al. [41]
Fh-HA (5 wt%)	3.6×10^{3}	1.1×10^{-2}	pH = 7.0 IS* = 0.01	Xue et al. [41]
Fh-HA (15 wt%)	2.7×10^{3}	8.8×10^{-3}	pH = 7.0 IS* = 0.01	Xue et al. [41]
Magnetite	1.4×10^{1}	1.0×10^{-1}	pH = 6.1 IS* = 0.01	Yean et al. [43]
Nano-magnetite	1.4×10^{2}	5.4×10^{-1}	pH = 6.1 IS* = 0.01	Yean et al. [43]
Goethite	1.7×10^{2}	4.0×10^{-2}	pH = 4 IS* = 0.01	Dixit et al. [32]
HFO	2.7×10^{2}	9.0×10^{-2}	pH = 4 IS* = 0.01	Dixit et al. [32]

*IS: ionic strength in mol L^{-1}

3.3. Speciation of Fe within the Fe-OM-Ca aggregates

The maximum amplitude of the EXAFS spectra was reached at 6.3 $Å^{-1}$ (Figure 3). The Fe(III)-oligomer reference displayed a close monotonous damping shape. ~~The Fh-like Np and Fh spectra showed a shoulder at 5.1 $Å^{-1}$ and an oscillation at 7.5 $Å^{-1}$ that was more pronounced for Fh compared to Fh-like Np.~~ The spectra of Fh-like Np and Fh showed a shoulder at 5.1 $Å^{-1}$ and an oscillation at 7.5 $Å^{-1}$. Both shoulder and oscillation were far more pronounced for Fh as compared to Fh-like Np. For Fe/OC = 0.02, the shape of the spectra were monotonous but a shoulder occurred at 7.5 $Å^{-1}$. For Fe/OC $\geq$ 0.05, the EXAFS spectra were more structured with an additional shoulder and a more pronounced shoulder occurring at 5.1 $Å^{-1}$ and 7.4 $Å^{-1}$, respectively.

For Fe/OC ≥ 0.05, the LCF reproduced ~~well~~ the EXAFS signal well. The percentage of nanoparticulate Fe, i.e. the percentage of Fe organized as Fh-like Np and Fh, was calculated from the LCF results (Table 3). ~~It~~ This value was ≥ 80% and increased with the increasing Ca/Fe ratio, as already reported [8]. For Fe/OC = 0.02, the LCF results ~~reported~~ returned ~70% of nanoparticulate Fe whatever the Ca/Fe ratio. However, the LCF exhibited a shoulder at 7.5 $Å^{-1}$ that was ~~much~~ more pronounced than in the experimental data (highlighted by the red arrow in Figure 3). This shoulder was mostly due to the neighbors siting at a distance larger than 3 Å (Figure SI-2). ~~Therefore, when the size of the Fe particle was smaller, it was expected that the shoulder at 7.5 $Å^{-1}$ would be less pronounced. This effect was observed for the Fh-like Np; the EXAFS spectrum exhibited a shoulder at 7.5 $Å^{-1}$ lower than Fh (Figure 3). The strongly pronounced shoulder at 7.5 $Å^{-1}$ provided evidence that the size of the Fe nanoparticle used for LCF is too large. This assumption was also supported by the size of the particulate Fe reported from the SAXS experiments showing that they were smaller for Fe/OC = 0.02 than for Fe/OC ≥ 0.05.~~ Therefore, it was expected that the shoulder at 7.5 $Å^{-1}$ would be less pronounced for a smaller Fe particle. This effect could be observed for the Fh-like Np which EXAFS spectrum exhibited a less intense shoulder at 7.5 $Å^{-1}$ than Fh (Figure 3). The strongly pronounced shoulder at 7.5 $Å^{-1}$ provided by the LCF evidenced that the size of the Fe nanoparticle used for the LCF was too large. This assumption was also supported by our previous study on the structural organization of Fe-OM aggregates in the presence of Ca showing that the size of the particulate Fe reported from the SAXS experiments showing that they were smaller for Fe/OC = 0.02 than for Fe/OC ≥ 0.05 [8].

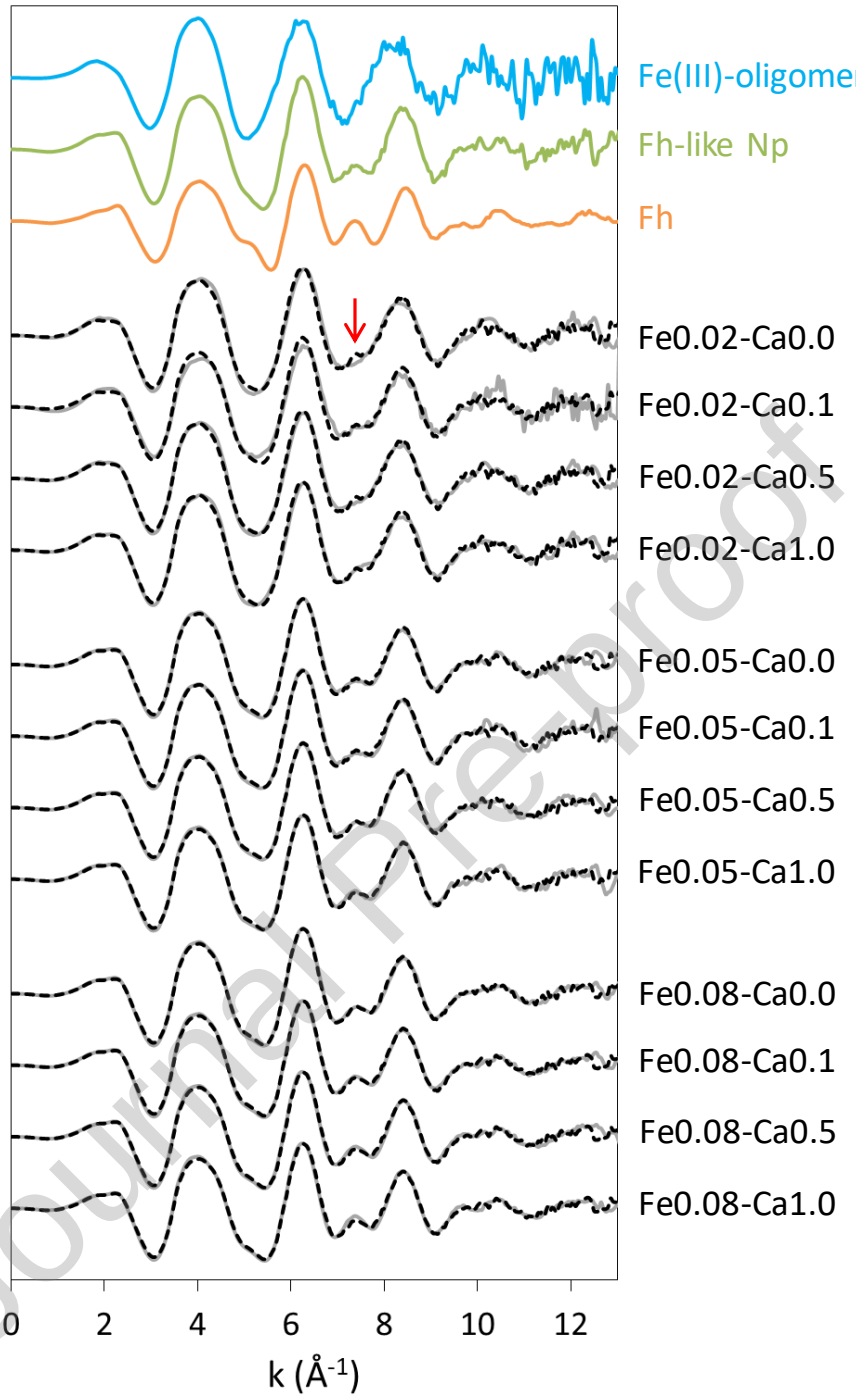

Figure 3 – Fe K-edge EXAFS spectra of the references used to perform the LCF and for each sample. The solid lines are experimental data and the dotted lines are the LCF results. The red arrow highlights the main discrepancy between the LCF result and the experimental data.

~~For Fe0.02-Ca1.0, the EXAFS signal was subtracted from the experimental data corresponding to 30% of the oligomers, as given by the LCF results. The signal is reported in Figure 4 along with the shell-by-shell fit result. The corresponding Fourier transform is reported in Figure SI-3a. The results of the fit (Table 4) showed 6.5 O at 1.98 Å and 1.6 Fe at~~

~~3.04 Å, in accordance with an Fh-like Np structure. However, 1.5 Fe at 3.47 Å were needed to fit the Np of Fe0.02-Ca1.0 versus 2.4 Fe for the Fh-like Np. This decrease in the number of second neighbors illustrates that the Fe0.02-Ca1.0 nanoparticles were smaller than the Fh-like Np nanoparticles. For Fe0.02-Ca0.05, the fit of the EXAFS signal, after 30% of the EXAFS signal for the Fe(III)-oligomers was subtracted from the experimental data returned 1 Fe at 3.04 Å (Figure SI-4 and Table SI-8). This low number of neighbors suggests that Fe(III)-oligomers remain in the signal as this amount of neighbors is too low to be provided by particulate Fe. The same is observed for Fe0.02-Ca0.0; the signal for these nanoparticles, after subtracting 30% of the Fe(III)-oligomers, exhibited less than 1 Fe (0.8) at 3.03 Å (Figure SI-5 and Table SI-8). These results demonstrate that the amount of Fe(III)-oligomers was underestimated by LCF in both samples. In order to isolate the EXAFS signal of the particulate Fe (i.e. a signal containing a comparable number of Fe first neighbors as in Fh and Fh-like Np), it is necessary to subtract 60% of the Fe(III)-oligomers (Figure 4) from Fe0.02-Ca0.5 and 70% of the Fe(III)-oligomers (Figure 4) from Fe0.02-Ca0.0. In both cases, the number of Fe at 3.47 Å was lower than for the Fh-like Nps, demonstrating that the Nps from Fe0.02-Ca0.0 and Fe0.02-Ca0.5 were smaller than the Fh-like Nps initially used for the LCF calculations.~~

In order to analyze the data for Fe/OC = 0.02, a procedure based on the linear combination principle was implemented. For Fe0.02-Ca1.0, the LCF reported that the Fe is constituted of 30% of Fe(III)-oligomers and 70% of Np. The experimental EXAFS signal (exp. EXAFS) of Fe0.02-Ca1.0 could be expressed as followed:

Exp. EXAFS = 0.3×(Fe(III)-oligomers EXAFS signal) + 0.7×(Np EXAFS signal)

However, the LCF results are not as convincing as for the samples with a Fe/OC ratio ≥ 0.05, as discussed above. The EXAFS signal of the Fe organized as Np within Fe0.02-Ca1.0 was extracted with the following procedure:

$$\text{Np EXAFS signal} = \frac{(\text{exp. EXAFS}) - 0.3 \times (\text{Fe(III)} - \text{oligomers EXAFS signal})}{0.7}$$

The obtained signal, denoted "Np from Fe0.02-Ca1.0", was fitted and reported in Figure 4 along with the shell-by-shell fit results. The corresponding Fourier transform was reported in Figure SI-3a. The results of the fit (Table 4) reported 6.5 O at 1.98 Å and 1.6 Fe at 3.04 Å, in accordance with an Fh-like Np structure. One can note 1.5 Fe at 3.47 Å were needed to fit the "Np from Fe0.02-Ca1.0" versus 2.4 Fe for the Fh-like Np. This decrease of second neighbors amount illustrated that the Fe0.02-Ca1.0 nanoparticles were smaller than the Fh-like Np nanoparticles. For Fe0.02-Ca0.5 and Fe0.02-Ca0.0, the same procedure was implemented (i.e. subtraction of 30% of Fe(III)-oligomers to the experimental data). However, the fit of the EXAFS signal obtained after the subtraction returned 1 Fe at 3.04 Å (Figure SI-4 and Table SI-8) and less than 1 Fe (0.8) at 3.03 Å (Figure SI-5 and Table SI-8) for Fe0.02-Ca0.5 and Fe0.02-Ca0.0, respectively. The low number of Fe neighbors suggested that signal from Fe(III)-oligomers remained in the signal after subtraction as this amount of neighbors is too low to be provided by (nano)particulate Fe. These results demonstrate that the amount of Fe(III)-oligomers was underestimated by LCF in both samples. In order to isolate the EXAFS signal of the particulate Fe (i.e. a signal containing a comparable number of Fe first neighbors as in Fh and Fh-like Np), it is necessary to subtract 60% of the Fe(III)-oligomers (Figure 4) from Fe0.02-Ca0.5 and 70% of Fe(III)-oligomers (Figure 4) from Fe0.02-Ca0.0. In both cases, the number of Fe at 3.47 Å was lower than for the Fh-like Nps, demonstrating that the Nps from Fe0.02-Ca0.0 and Fe0.02-Ca0.5 were smaller than the Fh-like Nps initially used for the LCF calculations.

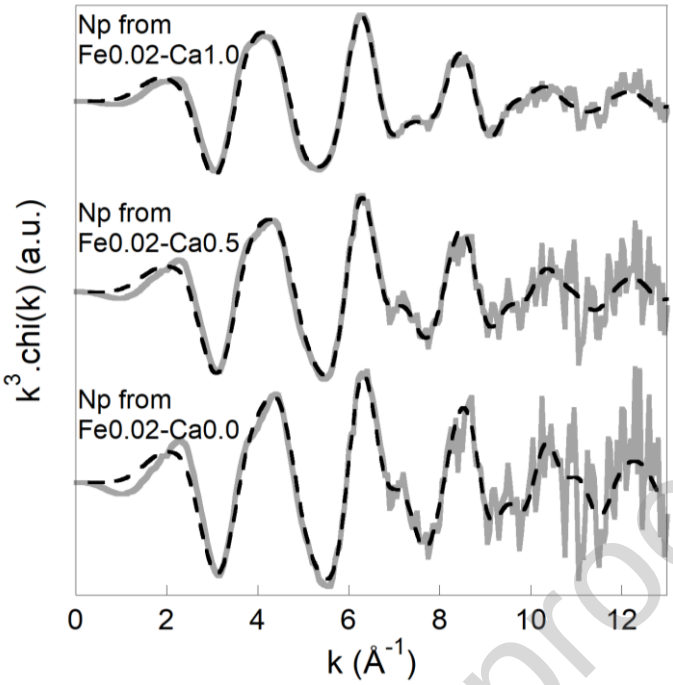

Figure 4 – Fe K-edge EXAFS spectra of the nanoparticulate Fe obtained by subtracting 30% of the EXAFS signal for the Fe(III)-oligomers from the raw signal of Fe0.02-Ca1.0, 60% from the raw signal of Fe0.02-Ca0.5 and 70% from the raw signal of Fe0.02-Ca0.0. The gray solid lines are the EXAFS signals after this subtraction and the black dotted lines are the fit results.

As a consequence, the proportion of the nanoparticulate Fe increased with ~~both the Fe/OC and Ca/Fe ratios~~ the Fe/OC and with the Ca/Fe ratio for Fe/OC = 0.02 (Table 3). This increased ratio is much more pronounced with the increasing Ca/Fe ratio for Fe/OC = 0.02 than for Fe/OC ≥ 0.05.

Table 3 – Percentage of Fh-like Nps. For Fe/OC ≥ 0.05, the % was calculated by LCF. For Fe/OC = 0.02, the % was deduced from the isolation of the Fh-like Nps EXAFS signal. The error is estimated to be ± 10%. n.d.: not determined

Fh-like Nps %		**Ca/Fe ratio**			
		0.0	**0.1**	**0.5**	**1.0**
Fe/OC	**0.02**	30	n.d.	40	70
	0.05	82	80	80	83
	0.08	85	86	87	88

Table 4 – Parameters used to fit the EXAFS signals at the Fe K-edge.

Sample		Fh-like Np	Fh	Np from Fe0.02-Ca0.0	Np from Fe0.02-Ca0.5	Np from Fe0.02-Ca1.0
Fe-O1	***N***	6.3	4.4	6.8	6.4	6.5
	***R* (Å)**	1.99	1.97	1.94	1.96	1.98
	σ²	0.009	0.010	0.007	0.008	0.010
Fe-Fe1	***N***	1.3	1.2	1.4	1.7	1.6
	***R* (Å)**	3.04	3.02	3.04	3.05	3.04
	σ²	0.009*	0.009*	0.007*	0.009*	0.010*
Fe-Fe2	***N***	2.4	3.5	2.1	2.0	1.5
	***R* (Å)**	3.47	3.47	3.50	3.48	3.47
	σ²	0.009*	0.009*	0.007*	0.009*	0.010*
Fe-O2	***N***	3.7**	4.7**	3.5**	3.7**	3.1**
	***R* (Å)**	3.63	3.61	3.70	3.66	3.69
	σ²	0.005	0.007	0.006	0.012	0.015
Fe-O3	***N***	4.0*	4.0*	4.0*	4.0*	4.0*
	***R* (Å)**	4.41	4.45	4.37	4.39	4.39
	σ²	0.015	0.015	0.002	0.006	0.010
R-factor ($\times10^{-3}$)		3.5	5.6	16.8	11.6	9.7

The amplitude reduction factor S_0^2 and the energy shift ΔE were set to 0.75 and -3.3 eV, respectively. *N* is the coordination number, *R* is the interatomic distance (Å) and *σ²* is the Debye-Weller factor. The error on *N*, *R* and *σ²* are usually estimated to be ± 10%, ± 1% and ± 20%, respectively. '*' denotes the fixed parameters. *The σ² were forced to be equal to each other. **The coordination number for the Fe-O2 path was constrained as follow~~ed~~s: $N_{Fe\text{-}O2} = N_{Fe\text{-}Fe1} + N_{Fe\text{-}Fe2}$.

3.4. Specific surface area

The SAXS curves displayed a shoulder between 10^{-2} and 10^{-1} $Å^{-1}$ providing evidence of the existence of Fe nanoparticles (Figure 5). The size of these Fe nanoparticles corresponded to Fe primary aggregates (radius between 2 and 5 nm) ~~comprised~~ assemblages of Fe primary beads (radius = 0.8 nm) [3,8]. However, the increase in the scattered intensity at low q indicates that the Fe nanoparticles ~~are~~ were aggregated ~~as~~ into larger objects [3,8]. For Fe/OC ≥ 0.05 and Ca/Fe ≥ 0.5, the shoulder is less pronounced indicating a dispersity in the Fe nanoparticle size and a high contribution of the larger objects to the total scattered intensity.

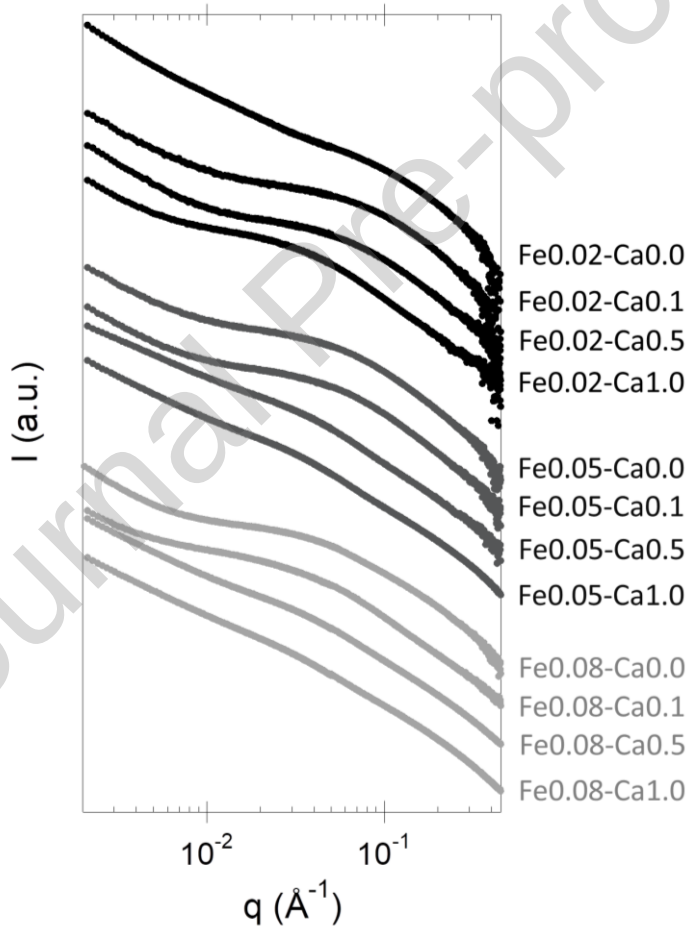

Figure 5 – SAXS curves obtained for all samples.

Without Ca, the SSA ~~remains~~ remained constant ~1300 m^2 g^{-1} irrespective of the Fe/OC ratio, as demonstrated by Guénet et al. [3] For Fe/OC = 0.02, the SSA ~~remains~~

remained constant while it increased with the increasing Ca/Fe ratio for Fe/OC ≥ 0.05 (Table 5).

Table 5 – Specific surface area (SSA, in $m^2 g^{-1}$) calculated for each sample. The errors on the parameters were 15%.

SSA ($m^2 g^{-1}$)		Ca/Fe			
		0.0	**0.1**	**0.5**	**1.0**
Fe/OC	**0.02**	1300	1100	1300	1300
	0.05	1250	1250	1650	1600
	0.08	1400	1800	2000	1700

4. Discussion

The huge structural transition from aggregates to a micrometric network observed for the Fe-OM aggregates in the presence of Ca is not accompanied by a dramatic evolution of their sorption capacity as we expected [8]. However, the impact of Ca is far more complex. Calcium interacts with the OM COOH sites that partially screen the interactions between Fe and OM [8]. As a consequence, the size of the Fh-like Nps increases, which should involve a decrease in their SSA and q_{max} [40,44–46]. Surprisingly, our results did not confirm these expectations: q_{max} and the SSA increased concomitantly with the increasing size of Fh-like Nps (Figure 6). Guénet et al. [3] assumed that these unexpected data result from the decrease in the OM coating of the Fe aggregates.

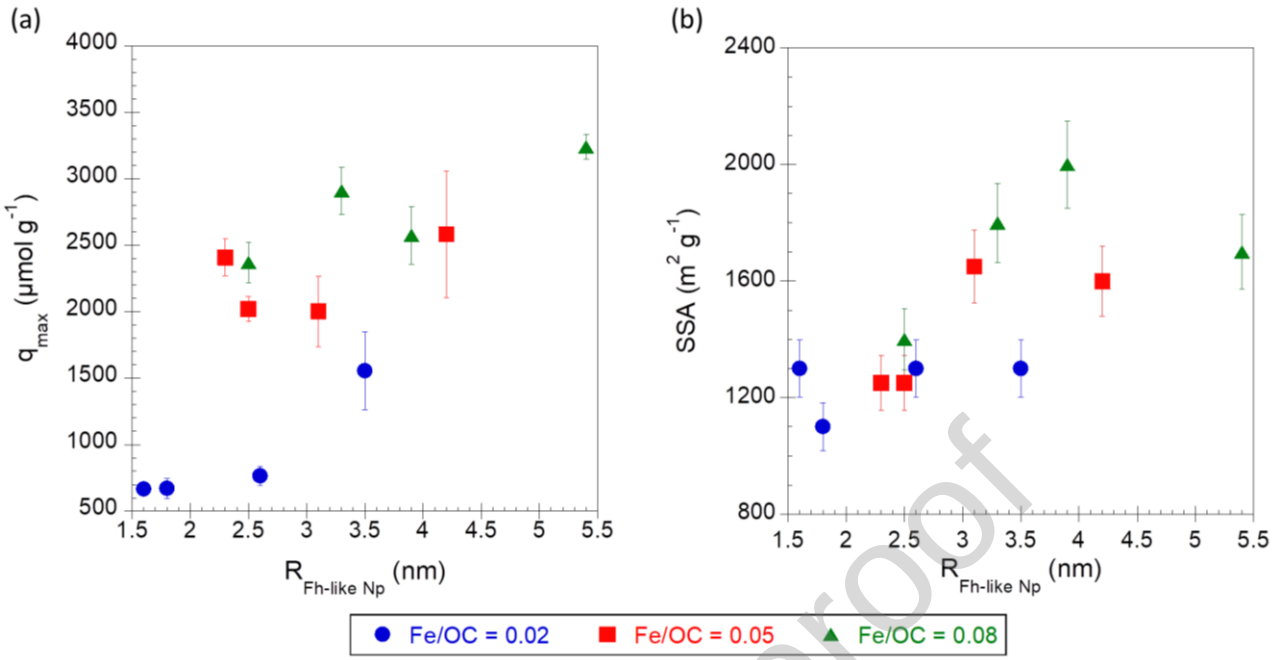

Figure 6 – Variations in (a) the As q_{max} calculated from the Langmuir isotherm and (b) the SSA relative to the radius of Fh-like Nps for Fe/OC = 0.02 (blue circles), 0.05 (red squares) and 0.08 (green triangles).

Since LHA is composed of 7.5×10^{-3} mol of COOH per gram of C [47], an apparent COOH concentration can be calculated for the >30 kDa fraction for each sample. Knowing the OM COOH density, the Fe and Ca concentrations in the >30 kDa fraction and given that Ca is bound to OM with a molar ratios $(COOH/Ca)_{>30\ kDa}$ = 3 (Beauvois et al. [8] and Figure SI 6), the quantity of available OM COOH that are able to bind the Fe phases can be calculated (Figure 7). For Fe/OC = 0.02, the SSA remained constant whereas for Fe/OC ≥ 0.05, the SSA tended to decrease with the increasing availability of the OM COOH sites.

In summary, at a high [Ca], the coating of the Fe phases by OM decreased and the site availability of the Fe phases increased.

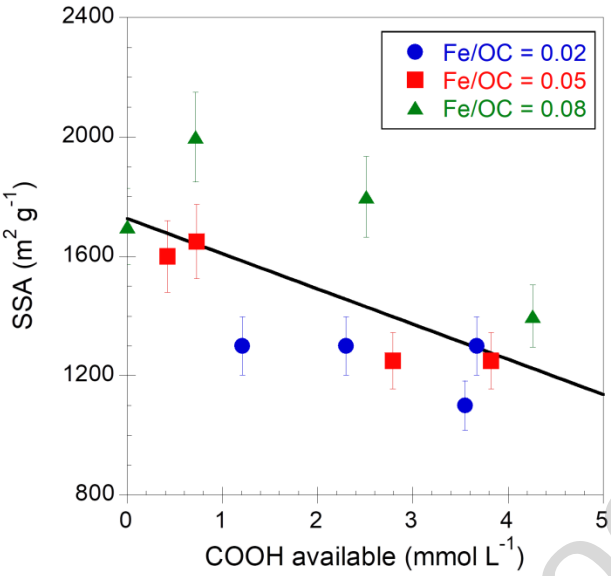

Figure 7 – Evolution of the SSA (m^2 g^{-1}) relative to the quantity of available COOH (mmol L^{-1}).

Another major parameter that controls the adsorption capacity of the Fe-OM aggregates is the Fe speciation (Figure 8). An exponential fit of the dataset demonstrated that when Fh-like Nps were not formed, As adsorption could occur through the Fe(III)-oligomers. This assumption was in agreement with previous results demonstrating that As binding by Fe(III) monomers or tetramers may ~~have occured~~ occur, leading to the formation of As-Fe-OM ternary complexes [48–50]. Thus, the adsorption capacity of Fe(III)-oligomers can ~~thus~~ be estimated as q_{max} ~250 µmol g^{-1} with a Langmuir K_{ads} value of ~20×10^{-3} L μmol^{-1}. The q_{max} value increases with the increasing Fh-like Np% which suggests that Fh-like Nps exhibit higher adsorption capacities than Fe(III)-oligomers. For the As-Fe-OM ternary complexes, in which the Fe speciation was dominated by the Fe(III)-oligomers, As is only bound to Fe as a bidentate mononuclear edge-sharing complex (^{2}E) due to geometric constraints [51]. For Fh-like Nps, As is bound as ^{2}E complexes and as bidentate binuclear corner-sharing (^{2}C) complexes [52]. Therefore, As can bind to Fh-like Nps in two ways as compared to Fe(III) oligomers. Moreover, the Fe vacancies in the Fh structure provide a higher density in terms of adsorption sites for Fh-like Nps than for Fe(III)-oligomers [52,53]. However, the Langmuir

K_{ads} value ~~decreased~~ decreases with the increasing Fh-like Nps % suggesting that As has higher affinity for Fe(III)-oligomers than for Fh-like Nps.

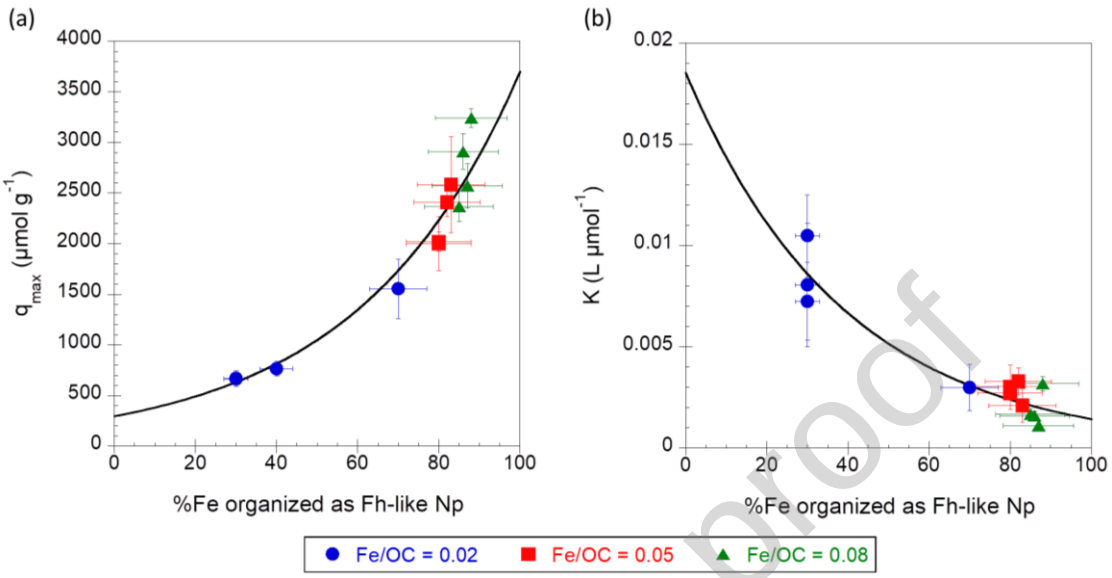

Figure 8 – Variations of (a) q_{max} and (b) Langmuir K_{ads} relative to the percentage of Fe organized as Fh-like Np for Fe/OC = 0.02 (blue circles), 0.05 (red squares) and 0.08 (green triangles).

As a consequence, the speciation of Fe impacts the oxidation-reduction behavior of the adsorbed As given that the formation of ^{2}E stabilizes As(III) ~~while~~ whereas the ^{2}C complexes lead to the oxidation of As(III) as As(V) [51]. Moreover, these results demonstrate that the speciation of Fe within the Fe-OM aggregates should thus be taken into account in order to evaluate and predict their ability to control metal(loid) mobility under environmental conditions. Since this distribution is dependent on the amounts of Ca and OM, their concentrations must be systematically determined. To reach this objective, the distribution of Fe between Fe(III)-oligomers and Fh-like Nps could, for example, be used to improve the existing geochemical models via the implementation of new parameters.

5. Conclusions

The overall reactivity of the Fe-OM aggregates strongly depends on their complex structural organization ~~that~~ which varies in the presence of Ca. In this study, we developed a complete description of the parameters that control the surface reactivity of Fe within synthesized Fe-OM-Ca aggregates using arsenic as a probe. We demonstrated that the Fe(III)-

oligomers and Fh-like Nps exhibit a high affinity for As and a high sorption capacity, respectively. The percentage of Fe distributed as Fe(III)-oligomers and Fh-like Nps is therefore a major parameter controlling As binding by Fe-OM aggregates. Moreover, our study provided evidence that Ca not only controls the ionic strength but also plays a significant role in the reactivity of the Fe-OM aggregates by acting as a competitor of Fe for binding OM. In that respect, the partial screening of the interaction between Fe and OM by Ca leads to an increase in the percentage of Fh-like Nps for low Fe/OC values and to the decrease in the Fh-like Nps coating rate by OM for high Fe/OC values. As a consequence, the availability of the Fe binding sites increases and the Fe-OM sorption capacity for As are enhanced by Ca. These results are of fundamental importance to model and predict As mobility in natural systems and will be efficient inputs to study As speciation and more specifically the oxidation state and thus the toxicity with oxidation-reduction cycles. Combined with our previous work [8], this study has emerged as an efficient approach to understand and predict the impact of Ca on the reactivity and mobility of Fe-OM aggregates in light of their structural organization. This global approach, applied to other element-Fe-OM interactions, will provide valuable information for understanding the pollution fate of natural systems.

Acknowledgments

This study is part of a thesis project funded by the French administrative region of Brittany and by the SOLEIL-LLB through the “ORPHREA” project. This study was funded by the French “Institut national des sciences de l'Univers” (INSU) through the “Initiative Structurante EC2CO – BIOHEFECT” allocated to Dr. Delphine Vantelon via the ‘ISAAP’ project. The authors acknowledge SOLEIL for beamtime allocation at the ROCK beamline (proposal 20170795) and SWING beamline (proposal 20181932) and the ROCK, SWING and LUCIA staff for their support. The work at ROCK was supported by a public grant overseen

by the French National Research Agency (ANR) as a part of the “Investissements d'Avenir” program ref: ANR-10-EQPX-45. Dr. Sara Mullin is acknowledged for post-editing the English style (https://www.proz.com/profile/677614).

References

[1] R. Kretzschmar, T. Schäfer, Metal Retention and Transport on Colloidal Particles in the Environment, Elements. 1 (2005) 205–210. https://doi.org/10.2113/gselements.1.4.205.

[2] N.S. Wigginton, K.L. Haus, M.F. Hochella Jr, Aquatic environmental nanoparticles, J. Environ. Monit. 9 (2007) 1306. https://doi.org/10.1039/b712709j.

[3] H. Guénet, M. Davranche, D. Vantelon, J. Gigault, S. Prévost, O. Taché, S. Jaksch, M. Pédrot, V. Dorcet, A. Boutier, J. Jestin, Characterization of iron–organic matter nano-aggregate networks through a combination of SAXS/SANS and XAS analyses: impact on As binding, Environ. Sci. Nano. 4 (2017) 938–954. https://doi.org/10.1039/C6EN00589F.

[4] M. Al-Sid-Cheikh, M. Pédrot, A. Dia, H. Guenet, D. Vantelon, M. Davranche, G. Gruau, T. Delhaye, Interactions between natural organic matter, sulfur, arsenic and iron oxides in re-oxidation compounds within riparian wetlands: NanoSIMS and X-ray adsorption spectroscopy evidences, Sci. Total Environ. 515–516 (2015) 118–128. https://doi.org/10.1016/j.scitotenv.2015.02.047.

[5] M. Pédrot, A. Dia, M. Davranche, M. Bouhnik-Le Coz, O. Henin, G. Gruau, Insights into colloid-mediated trace element release at the soil/water interface, J. Colloid Interface Sci. 325 (2008) 187–197. https://doi.org/10.1016/j.jcis.2008.05.019.

[6] G. Ratié, D. Vantelon, E. Lotfi Kalahroodi, I. Bihannic, A.C. Pierson-Wickmann, M. Davranche, Iron speciation at the riverbank surface in wetland and potential impact on the mobility of trace metals, Sci. Total Environ. 651 (2019) 443–455. https://doi.org/10.1016/j.scitotenv.2018.09.143.

[7] C. Poggenburg, R. Mikutta, M. Sander, A. Schippers, A. Marchanka, R. Dohrmann, G. Guggenberger, Microbial reduction of ferrihydrite-organic matter coprecipitates by Shewanella putrefaciens and Geobacter metallireducens in comparison to mediated electrochemical reduction, Chem. Geol. 447 (2016) 133–147. https://doi.org/10.1016/j.chemgeo.2016.09.031.

[8] A. Beauvois, D. Vantelon, J. Jestin, C. Rivard, M. Bouhnik-Le Coz, A. Dupont, V. Briois, T. Bizien, A. Sorrentino, B. Wu, M.-S. Appavou, E. Lotfi-Kalahroodi, A.-C. Pierson-Wickmann, M. Davranche, How does calcium drive the structural organization of iron–organic matter aggregates? A multiscale investigation, Environ. Sci. Nano. (2020) 10.1039.D0EN00412J. https://doi.org/10.1039/D0EN00412J.

[9] L. Gentile, T. Wang, A. Tunlid, U. Olsson, P. Persson, Ferrihydrite Nanoparticle Aggregation Induced by Dissolved Organic Matter, J. Phys. Chem. A. 122 (2018) 7730–7738. https://doi.org/10.1021/acs.jpca.8b05622.

[10] M. Pédrot, A.L. Boudec, M. Davranche, A. Dia, O. Henin, How does organic matter constrain the nature, size and availability of Fe nanoparticles for biological reduction?, J. Colloid Interface Sci. 359 (2011) 75–85. https://doi.org/10.1016/j.jcis.2011.03.067.

[11] D. Vantelon, M. Davranche, R. Marsac, C. La Fontaine, H. Guénet, J. Jestin, G. Campaore, A. Beauvois, V. Briois, Iron speciation in iron-organic matter nanoaggregates: A kinetic approach coupling Quick-EXAFS and MCR-ALS

chemometry, Environ. Sci. Nano. 6 (2019) 2641–2651. https://doi.org/10.1039/C9EN00210C.
[12] T. Karlsson, P. Persson, Complexes with aquatic organic matter suppress hydrolysis and precipitation of Fe(III), Chem. Geol. 322–323 (2012) 19–27. https://doi.org/10.1016/j.chemgeo.2012.06.003.
[13] T. Karlsson, P. Persson, U. Skyllberg, C.-M. Mörth, R. Giesler, Characterization of Iron(III) in Organic Soils Using Extended X-ray Absorption Fine Structure Spectroscopy, Environ. Sci. Technol. 42 (2008) 5449–5454. https://doi.org/10.1021/es800322j.
[14] M. Kleber, K. Eusterhues, M. Keiluweit, C. Mikutta, R. Mikutta, P.S. Nico, Mineral–Organic Associations: Formation, Properties, and Relevance in Soil Environments, in: Adv. Agron., Elsevier, 2015: pp. 1–140. https://doi.org/10.1016/bs.agron.2014.10.005.
[15] C. Chen, J.J. Dynes, J. Wang, D.L. Sparks, Properties of Fe-Organic Matter Associations via Coprecipitation versus Adsorption, Environ. Sci. Technol. 48 (2014) 13751–13759. https://doi.org/10.1021/es503669u.
[16] T. Karlsson, P. Persson, Coordination chemistry and hydrolysis of Fe(III) in a peat humic acid studied by X-ray absorption spectroscopy, Geochim. Cosmochim. Acta. 74 (2010) 30–40. https://doi.org/10.1016/j.gca.2009.09.023.
[17] J.M. Zachara, C.T. Resch, S.C. Smith, Influence of humic substances on Co2+ sorption by a subsurface mineral separate and its mineralogic components, Geochim. Cosmochim. Acta. 58 (1994) 553–566. https://doi.org/10.1016/0016-7037(94)90488-X.
[18] C. Bruggeman, D.J. Liu, N. Maes, Influence of Boom Clay organic matter on the adsorption of Eu $^{3+}$ by illite – geochemical modelling using the component additivity approach, Radiochim. Acta. 98 (2010) 597–605. https://doi.org/10.1524/ract.2010.1759.
[19] A.W.P. Vermeer, J.K. McCulloch, W.H. van Riemsdijk, L.K. Koopal, Metal Ion Adsorption to Complexes of Humic Acid and Metal Oxides: Deviations from the Additivity Rule, Environ. Sci. Technol. 33 (1999) 3892–3897. https://doi.org/10.1021/es990260k.
[20] H. Lippold, J. Lippmann-Pipke, Effect of humic matter on metal adsorption onto clay materials: Testing the linear additive model, J. Contam. Hydrol. 109 (2009) 40–48. https://doi.org/10.1016/j.jconhyd.2009.07.009.
[21] N. Janot, P.E. Reiller, M.F. Benedetti, Modelling Eu(III) speciation in a Eu(III)/PAHA/α-Al2O3 ternary system, Colloids Surf. Physicochem. Eng. Asp. 435 (2013) 9–15. https://doi.org/10.1016/j.colsurfa.2013.02.052.
[22] T. Saito, L.K. Koopal, S. Nagasaki, S. Tanaka, Analysis of Copper Binding in the Ternary System Cu^{2+}/Humic Acid/Goethite at Neutral to Acidic pH, Environ. Sci. Technol. 39 (2005) 4886–4893. https://doi.org/10.1021/es0500308.
[23] L. Weng, W.H. Van Riemsdijk, T. Hiemstra, Effects of Fulvic and Humic Acids on Arsenate Adsorption to Goethite: Experiments and Modeling, Environ. Sci. Technol. 43 (2009) 7198–7204. https://doi.org/10.1021/es9000196.
[24] I. Christl, R. Kretzschmar, Interaction of copper and fulvic acid at the hematite-water interface, Geochim. Cosmochim. Acta. 65 (2001) 3435–3442. https://doi.org/10.1016/S0016-7037(01)00695-0.
[25] A. Iglesias, R. López, S. Fiol, J.M. Antelo, F. Arce, Analysis of copper and calcium–fulvic acid complexation and competition effects, Water Res. 37 (2003) 3749–3755. https://doi.org/10.1016/S0043-1354(03)00236-7.
[26] C.C. Davis, M. Edwards, Role of Calcium in the Coagulation of NOM with Ferric Chloride, Environ. Sci. Technol. 51 (2017) 11652–11659. https://doi.org/10.1021/acs.est.7b02038.

[27] M. Grafe, M.J. Eick, P.R. Grossl, Adsorption of Arsenate (V) and Arsenite (III) on Goethite in the Presence and Absence of Dissolved Organic Carbon, Soil Sci. Soc. Am. J. 65 (2001) 1680–1687. https://doi.org/10.2136/sssaj2001.1680.
[28] D. Dickson, G. Liu, Y. Cai, Adsorption kinetics and isotherms of arsenite and arsenate on hematite nanoparticles and aggregates, J. Environ. Manage. 186 (2017) 261–267. https://doi.org/10.1016/j.jenvman.2016.07.068.
[29] K.P. Raven, A. Jain, R.H. Loeppert, Arsenite and Arsenate Adsorption on Ferrihydrite: Kinetics, Equilibrium, and Adsorption Envelopes, Environ. Sci. Technol. 32 (1998) 344–349. https://doi.org/10.1021/es970421p.
[30] A. Dia, G. Gruau, G. Olivié-Lauquet, C. Riou, J. Molénat, P. Curmi, The distribution of rare earth elements in groundwaters: assessing the role of source-rock composition, redox changes and colloidal particles, Geochim. Cosmochim. Acta. 64 (2000) 4131–4151. https://doi.org/10.1016/S0016-7037(00)00494-4.
[31] G. Olivie-Lauquet, Release of Trace Elements in Wetlands: Role of Seasonal Variability, Water Res. 35 (2001) 943–952. https://doi.org/10.1016/S0043-1354(00)00328-6.
[32] S. Dixit, J.G. Hering, Comparison of Arsenic(V) and Arsenic(III) Sorption onto Iron Oxide Minerals: Implications for Arsenic Mobility, Environ. Sci. Technol. 37 (2003) 4182–4189. https://doi.org/10.1021/es030309t.
[33] L. Hao, M. Liu, N. Wang, G. Li, A critical review on arsenic removal from water using iron-based adsorbents, RSC Adv. 8 (2018) 39545–39560. https://doi.org/10.1039/C8RA08512A.
[34] D.L. Sparks, Environmental soil chemistry, 2nd ed, Academic Press, Amsterdam ; Boston, 2003.
[35] V. Briois, C. La Fontaine, S. Belin, L. Barthe, T. Moreno, V. Pinty, A. Carcy, R. Girardot, E. Fonda, ROCK: the new Quick-EXAFS beamline at SOLEIL, J. Phys. Conf. Ser. 712 (2016) 012149. https://doi.org/10.1088/1742-6596/712/1/012149.
[36] U. Schwertmann, R.M. Cornell, eds., Iron Oxides in the Laboratary, Wiley-VCH Verlag GmbH, Weinheim, Germany, 2000. https://doi.org/10.1002/9783527613229.
[37] B. Ravel, M. Newville, *ATHENA* , *ARTEMIS* , *HEPHAESTUS* : data analysis for X-ray absorption spectroscopy using *IFEFFIT*, J. Synchrotron Radiat. 12 (2005) 537–541. https://doi.org/10.1107/S0909049505012719.
[38] J.-L. Hazemann, J.F. Bérar, A. Manceau, Rietveld Studies of the Aluminium-Iron Substitution in Synthetic Goethite, Mater. Sci. Forum. 79–82 (1991) 821–826. https://doi.org/10.4028/www.scientific.net/MSF.79-82.821.
[39] M. Newville, EXAFS analysis using *FEFF* and *FEFFIT*, J. Synchrotron Radiat. 8 (2001) 96–100. https://doi.org/10.1107/S0909049500016290.
[40] A. Hofmann, M. Pelletier, L. Michot, A. Stradner, P. Schurtenberger, R. Kretzschmar, Characterization of the pores in hydrous ferric oxide aggregates formed by freezing and thawing, J. Colloid Interface Sci. 271 (2004) 163–173. https://doi.org/10.1016/j.jcis.2003.11.053.
[41] Q. Xue, Y. Ran, Y. Tan, C.L. Peacock, H. Du, Arsenite and arsenate binding to ferrihydrite organo-mineral coprecipitate: Implications for arsenic mobility and fate in natural environments, Chemosphere. 224 (2019) 103–110. https://doi.org/10.1016/j.chemosphere.2019.02.118.
[42] J. Zhu, M. Pigna, V. Cozzolino, A.G. Caporale, A. Violante, Sorption of arsenite and arsenate on ferrihydrite: Effect of organic and inorganic ligands, J. Hazard. Mater. 189 (2011) 564–571. https://doi.org/10.1016/j.jhazmat.2011.02.071.

[43] S. Yean, L. Cong, C.T. Yavuz, J.T. Mayo, W.W. Yu, A.T. Kan, V.L. Colvin, M.B. Tomson, Effect of magnetite particle size on adsorption and desorption of arsenite and arsenate, J. Mater. Res. 20 (2005) 3255–3264. https://doi.org/10.1557/jmr.2005.0403.
[44] H. Wang, F. Shadman, Effect of particle size on the adsorption and desorption properties of oxide nanoparticles, AIChE J. 59 (2013) 1502–1510. https://doi.org/10.1002/aic.13936.
[45] X. Wang, W. Li, R. Harrington, F. Liu, J.B. Parise, X. Feng, D.L. Sparks, Effect of Ferrihydrite Crystallite Size on Phosphate Adsorption Reactivity, Environ. Sci. Technol. 47 (2013) 10322–10331. https://doi.org/10.1021/es401301z.
[46] T. Hiemstra, J.C. Mendez, J. Li, Evolution of the reactive surface area of ferrihydrite: time, pH, and temperature dependency of growth by Ostwald ripening, Environ. Sci. Nano. 6 (2019) 820–833. https://doi.org/10.1039/C8EN01198B.
[47] J.D. Ritchie, E.M. Perdue, Proton-binding study of standard and reference fulvic acids, humic acids, and natural organic matter, Geochim. Cosmochim. Acta. 67 (2003) 85–96. https://doi.org/10.1016/S0016-7037(02)01044-X.
[48] M. Hoffmann, C. Mikutta, R. Kretzschmar, Arsenite Binding to Natural Organic Matter: Spectroscopic Evidence for Ligand Exchange and Ternary Complex Formation, Environ. Sci. Technol. 47 (2013) 12165–12173. https://doi.org/10.1021/es4023317.
[49] C. Mikutta, R. Kretzschmar, Spectroscopic Evidence for Ternary Complex Formation between Arsenate and Ferric Iron Complexes of Humic Substances, Environ. Sci. Technol. 45 (2011) 9550–9557. https://doi.org/10.1021/es202300w.
[50] C. Catrouillet, M. Davranche, A. Dia, M. Bouhnik-Le Coz, E. Demangeat, G. Gruau, Does As(III) interact with Fe(II), Fe(III) and organic matter through ternary complexes?, J. Colloid Interface Sci. 470 (2016) 153–161. https://doi.org/10.1016/j.jcis.2016.02.047.
[51] H. Guénet, M. Davranche, D. Vantelon, M. Pédrot, M. Al-Sid-Cheikh, A. Dia, J. Jestin, Evidence of organic matter control on As oxidation by iron oxides in riparian wetlands, Chem. Geol. 439 (2016) 161–172. https://doi.org/10.1016/j.chemgeo.2016.06.023.
[52] G. Ona-Nguema, G. Morin, F. Juillot, G. Calas, G.E. Brown, EXAFS Analysis of Arsenite Adsorption onto Two-Line Ferrihydrite, Hematite, Goethite, and Lepidocrocite, Environ. Sci. Technol. 39 (2005) 9147–9155. https://doi.org/10.1021/es050889p.
[53] J.L. Jambor, J.E. Dutrizac, Occurrence and Constitution of Natural and Synthetic Ferrihydrite, a Widespread Iron Oxyhydroxide, Chem. Rev. 98 (1998) 2549–2586. https://doi.org/10.1021/cr970105t.

Statement of contributions

Delphine Vantelon: PhD thesis co-supervisor

Jacques Jestin: PhD thesis co-supervisor

Martine Bouhnik-Le Coz: contribution in performing and analysing ICP-MS measurements

Charlotte Catrouillet: contribution in performing and analysing ICP-MS measurements

Valérie Briois: local contact at ROCK beamline (SOLEIL synchrotron) for collecting XAS at Fe K-edge, support to XAS data analysis

Thomas Bizien: local contact at SWING beamline (SOLEIL synchrotron) for collecting small-angle X-rays scattering (SAXS), support to SAXS data treatment

Mélanie Davranche: PhD thesis co-supervisor

Declaration of interests

☒ The authors declare that they have no known competing financial interests or personal relationships that could have appeared to influence the work reported in this paper.

☐The authors declare the following financial interests/personal relationships which may be considered as potential competing interests:

Highlights

- Ca improves iron-organic matter (Fe-OM) aggregate sorption capacities.
- Ca drives the Ferrihydrite-like nanoparticles (Fh-like Nps) amount for low Fe/OC.
- Ca drives the Fh-like Np adsorption capacity for high Fe/OC.
- As adsorption is controlled by Fe speciation within Fe-OM aggregates.
- As binding affinity is higher for Fe(III)-oligomers than for Fh-like Nps.